Flexible Holey Graphene Paper Electrodes with Enhanced Rate Capability for Energy Storage Applications

Xin Zhao, Cary M. Hayner, Mayfair C. Kung, and Harold H. Kung*

Chemical and Biological Engineering Department, Northwestern University, Evanston, Illinois 60208-3120, United States

ABSTRACT The unique combination of high surface area, high electrical conductivity and robust mechanical integrity has attracted great interest in the use of graphene sheets for future electronics applications. Their potential applications for high-power energy storage devices, however, are restricted by the accessible volume, which may be only a fraction of the physical volume, a consequence of the compact geometry of the stack and the ion mobility. Here we demonstrated that remarkably enhanced power delivery can be realized in graphene papers for the use in Li-ion batteries by controlled generation of in-plane porosity *via* a mechanical cavitation-chemical oxidation approach. These flexible, holey graphene papers, created via facile microscopic engineering, possess abundant ion binding sites, enhanced ion diffusion kinetics, and excellent high-rate lithium-ion storage capabilities, and are suitable for high-performance energy storage devices.

KEYWORDS: holey · graphene · defects · electrode · Li-ion battery

INTRODUCTION

Recently, there has been an intensive effort to investigate the use of graphene sheet stacks as electrical energy storage materials.[1−5] These studies include control of their architecture *via* surfactant assisted assembly,[6] coupling with nanofibres to form three-dimensional battery electrodes,[7] and composite formation with oxides or polymers for supercapacitor electrodes applications.[8−11] Modification by doping with boron or nitrogen[12,13] or functionalization[14] in order to enhance the storage capacity has also been attempted. The accelerated pace of research activities is prompted by the recognition that graphene possesses distinct properties as electrical energy storage material. The extremely high in-plane electrical conductivities[15,16] and the excellent tensile modulus and mechanical durability[17] of self-supporting graphene papers could eliminate the requirement of traditional inactive additives and metal foil current collectors, which in turn permits flexibility in novel geometric designs.[18] Their elastic nature also permits accommodation of large volume variations that occur during charge/discharge cycling of embedded high-capacity metallic or redox materials, thereby minimizing electrode destruction from the associated strain.[19−22]

However, the extremely large aspect ratio of graphene sheets places constraint on the practical capacity of graphene-based electrodes at high charge/discharge rates.[23,24] During drying of randomly stacked graphene sheets, the surface tension of the retreating liquid meniscus collapses the spacing between sheets and leads to intimate van der Waals contact between them, hence reducing open porosity. Thermally annealed graphene stacks show severe intersheet aggregation that limits permeation of electrolyte between the layers. Thus, in spite of a high in-plane Li diffusion coefficient of $\sim 10^{-8}$ cm^2/s,[25] cross-plane diffusivity is low, and Li migration into and out of a graphene stack is restricted to stack edges.[26−28] To address the inferior power delivery of graphene electrodes, vertically oriented design of graphene stacks with a preponderance of exposed edge planes and enlarged interlayer spacing was constructed and examined.[29−31] However, these submicrometer-thick, fragile electrodes cannot achieve sufficient long-term reliability or high overall charge-storage capacity due to a low mass loading of the active components. The labor-intensive fabrication involved also poses a challenge for cost-effective production of the electrodes.

We report here a conceptually different approach to enhance the power capability of graphene-based electrodes, by introducing in-plane carbon vacancy defects (pores) into graphene sheets using a facile solution method that affords a broad, tunable range

* Address correspondence to hkung@northwestern.edu.

Received for review July 18, 2011 and accepted October 8, 2011.

Published online October 08, 2011
10.1021/nn202710s

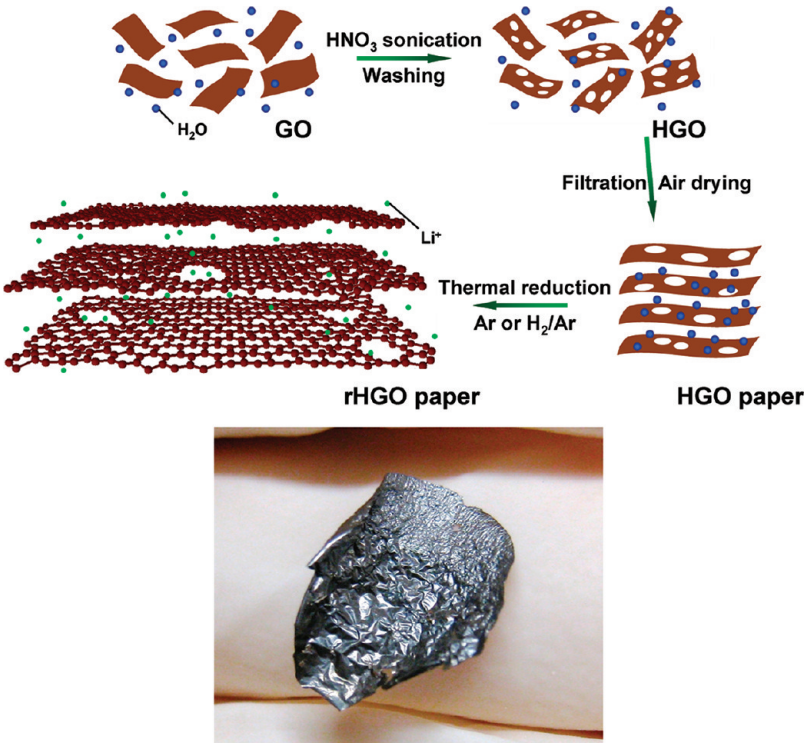

Figure 1. Schematic drawing (not to scale) of the introduction of in-plane pores into chemically exfoliated graphene oxide (GO) and the subsequent filtration into a holey graphene oxide paper (HGO). The thermal reduction of graphene oxide sheets with in-plane porosity and removal of water molecules (blue spheres) from the interlayers result in a 3-D network with interconnecting graphitic domains that retain high electrical conductivity and structural integrity and disordered porous graphene regions that provide interplane diffusion channels (rHGO). Li ions (green spheres) can diffuse throughout the structure rapidly through the in-plane pores and interplane channels. The interlayer spacing between graphene sheets is greatly exaggerated. The digital image shows a coin cell-size Ar-rHGO-III paper.

of defect dimensions. These in-plane pores provide a high density of new, cross-plane ion diffusion channels that facilitate charge transport and storage at high rates. Combining this with a 3-D graphitic architecture that maintains superior electrical conductivity and structural integrity, a novel form of graphene electrode is generated, which is capable of ultrahigh power delivery. The method can be extended to rational design of holey graphene and its hybrids with new functionalities.

RESULTS AND DISCUSSION

In-plane porosity was introduced into the basal planes of graphene oxide (GO) *via* a wet chemical method that combined ultrasonic vibration and mild acid oxidation, as shown in Figure 1. It has been reported that a combination of ultrasonic vibration and concentrated acid generated defects on CNT sidewalls and cut CNTs into shorter fullerene pipes.[32−34] Sonication of GO in hot HNO_3 also led to scissoring of GO into soluble polyaromatic hydrocarbons.[35] We employed a milder condition by reducing the acid concentration and shortening the sonication period, so as to obtain a better control of the defect generation process. Chemically exfoliated GO prepared *via* a modified Hummers method[36] was suspended in water (0.1% w/w), and mixed with a desired amount of 70% concentrated HNO_3 under stirring. The mixtures were then subjected to continuous bath sonication at room temperature for 1 h. The ultrasound at sufficient acoustic pressures creates high strain rates and frictional forces in cavitation bubbles that attack the carbonaceous surface and break the framework.[35,37−39] The HNO_3 then reacts with the coordinatively unsaturated carbon atoms at the damage sites and existing edge sites of the GO, resulting in partial detachment and removal of carbon atoms from the GO sheet. Four solutions of increasing acid concentrations were tested, corresponding to a GO suspension/70% HNO_3 volume ratio of 1:5, 1:7.5, 1:10, and 1:12.5. The resulting holey graphene oxide (HGO) are labeled HGO-I, II, III, and IV, respectively.

The aqueous suspensions of washed HGO were dropped onto Si wafers for SEM characterization. The stacked layers of HGO-I appeared to be continuous, similar to GO. The pores were probably too small and/or the contrast too weak to be observable at these conditions. With increasing degree of oxidation, large holes of increasing sizes, easily observable with SEM, became noticeable on HGO-II to -IV (Figure 2). Smaller holes, observable with TEM but not SEM used here, also increased in density (Figure 3). Clearly, the oxidation

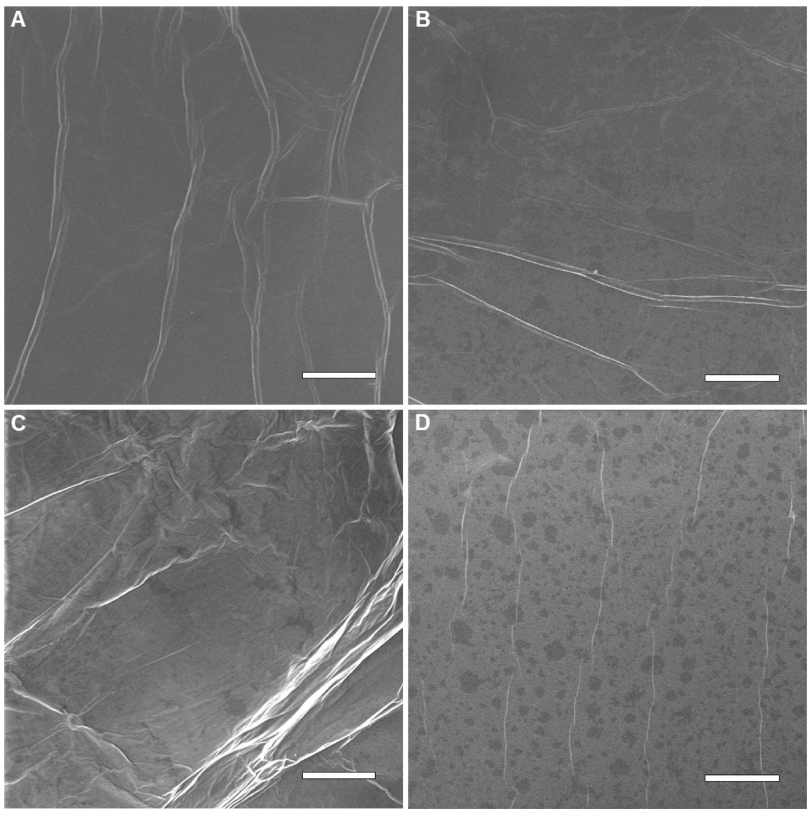

Figure 2. SEM images of holey graphene oxide sheets deposited on Si wafers: (A) HGO-I, (B) HGO-II, (C) HGO-III, and (D) HGO-IV. Scale bar is 20 μm.

procedure generated holey defects of a wide size distribution. The XPS C1s and O1s spectra of GO, published previously,[40] could be deconvoluted into various components corresponding to carbon and oxygen atoms in different functional groups,[41,42] consistent with considerable degrees of oxidation. The sum of the intensities of all C1s peaks assigned to oxygen functional groups,[42,43] in particular the epoxy/alkoxy carbon (C−O) and the carbonyl carbon (C═O) groups, increased dramatically for samples treated with higher concentrations of acid. Simultaneously, the peak intensity of aromatic C−C bonds decreased. From the areas of the four C1s components, it was estimated that ~65% of all carbon atoms in GO were sp^2 carbon, while this fraction decreased to ~61% for HGO-I and ~46% for HGO-IV. The characteristic peak assigned to C−O in the O1s spectrum became visibly less intense after the acid treatment, while the peak intensities of the O−C═O and C═O components became much more prominent in HGO than in GO papers. These results suggested enrichment of carbonyl and carboxylate groups in HGO.[35]

In an attempt to gain more structural information of these pores by visualization, we made use of the interaction of Pd ions with surface functional groups, especially carboxylate groups, which are expected to be localized heavily at the defects and edges of GO sheets. Thus, GO and HGO suspensions were mixed with diluted $Pd(OAc)_2$ aqueous solutions, and the suspension was allowed to settle overnight. Afterward, the solid was separated by centrifugation and then examined by TEM, when the Pd ions were reduced by the electron beam to form Pd nanosize aggregates. On GO, Pd particles were found to assemble preferentially along the edges, although some were randomly distributed on the basal planes (Figure 3A). For the HGO samples, the density of Pd particles on the basal plane increased with increasing severity of acid treatment (Figure 3B−H). This is consistent with conclusions from the XPS measurements. For HGO-III and -IV, rings of crystalline Pd particles, ~2 nm in diameter, were detected on the basal planes (Figure 3E and F). We reasoned that these rings identified the locations of the in-plane defects, since the edges of the pores were populated with carboxylate groups where the Pd ions were bound to. The successful binding of Pd ions also illustrates that the HGO can act as a substrate for growing and anchoring other nanostructured materials.

Thermal reduction of a free-standing, air-dried GO or HGO paper at 700 °C in a flow of either Ar or a H_2 (10%)/Ar (90%) mixture produced an electrically conducting 3-D scaffold with retention of the paper form. The scaffold consisted of three-dimensionally connected graphitic domains reconstituted from partial overlap and coalescing of graphene sheets, and pockets formed from rapid evaporation of water trapped between sheets

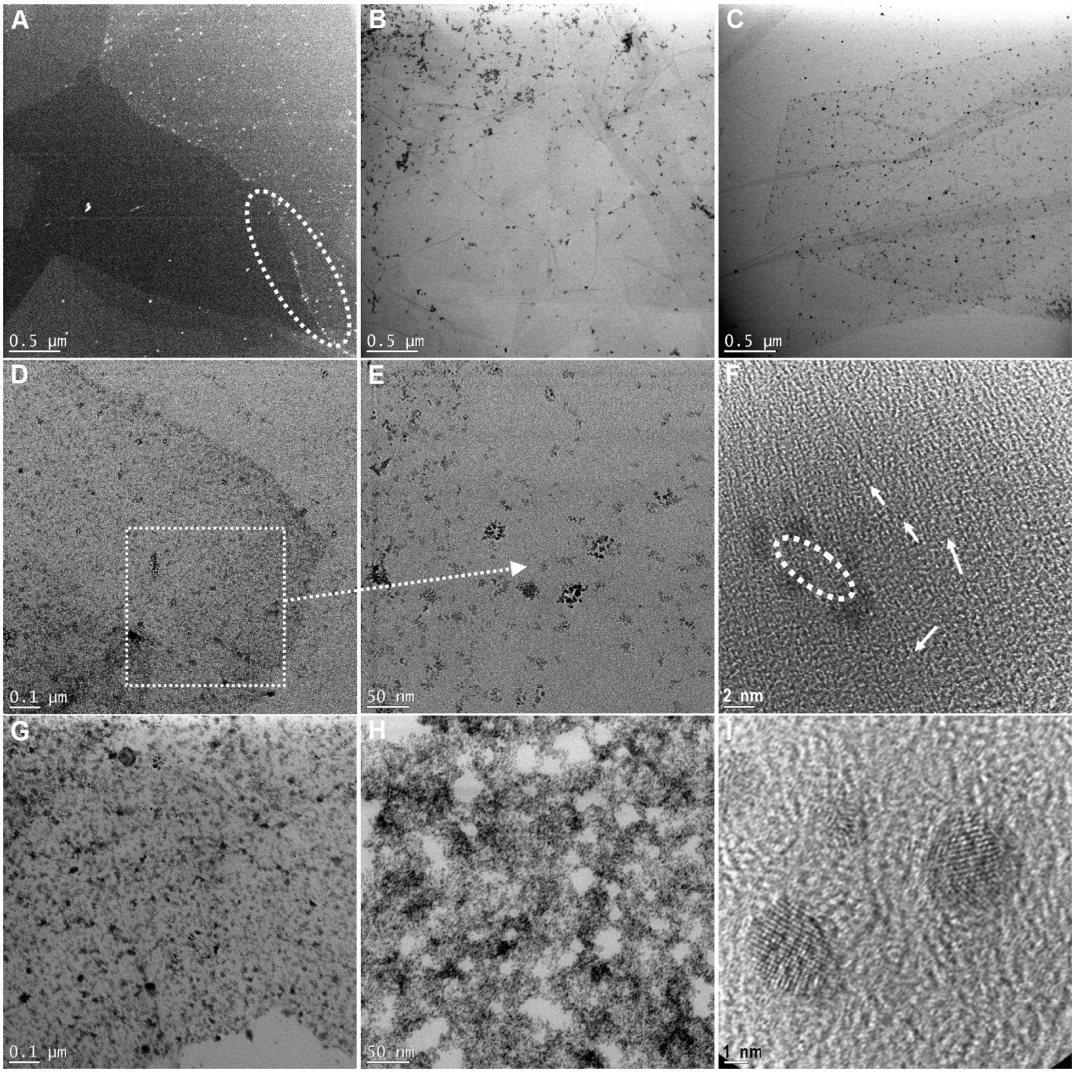

Figure 3. TEM images of Pd-stained graphene oxide sheets: (A) Z-contrast image of GO. Circled region shows Pd particles deposited along the sheet edges, (B) HGO-I, (C) HGO-II, (D) HGO-III, (E) a high-magnification image of the highlighted region in (D) showing Pd particles in ring-shape arrangements, a result of the Pd ion binding to carboxylate at pore perimeters,[40] (F) a high-magnification image of Pd clusters in a single ring arrangement surrounding a pore in the center. Arrows indicate the crystalline regions of HGO, (G) HGO-IV, (H) HGO-IV at higher magnification, showing the highly porous HGO structure, (I) a high-magnification image of crystalline, 2−3 nm Pd particles on a basal plane.

during heating. The in-plane porosity of HGO was retained after thermal reduction (Figure 4). Removal of most oxygen functional groups by reduction was verified by XPS in reduced HGO (rHGO) papers (Figure 5), and both C1s and O1s spectra showed that the Ar-reduced HGO (Ar-rHGO) papers possessed higher contents of C═O groups than the H_2-reduced (H-rHGO) counterparts. It is reasonable to expect that reduction in H_2 is more effective than in Ar, thus resulting in more extensive removal of oxygenated groups.

From the SEM images, there was a general observation that the size of the visible pores in a rHGO sample increased with the severity of acid treatment. The largest pores in the Ar-rHGO samples were estimated to be roughly 7, 20, 80, and 600 nm for samples I, II, III, and IV, respectively. In general, it was easier to locate larger pores in samples reduced in Ar than those reduced in H_2. For example, 500−600 nm pores were found readily in Ar-rHGO-IV (Figure 4H), whereas most of the pores found in H-rHGO-IV showed mostly 200−300 nm pores (Figure 4I). One contribution to the difference in pore size between Ar- and H_2-reduced samples is as follows. Reduction in Ar was accomplished by decomposition of epoxy and carboxylate groups and release of CO_2 and/or CO molecules. Consequently, significant loss of carbon and atomic rearrangement took place when reduced in Ar and would be the most severe for a sample of the highest initial oxygen content.[43] For reduction in H_2, however, there was the competing reaction of hydrogenation of these groups to remove the oxygen atoms as water and return the carbon atoms to the graphene sheet,[41,43] which could reduce the in-plane pores size. Thus, the Ar-rHGO papers show larger pores and more apparent topological deformation[44]

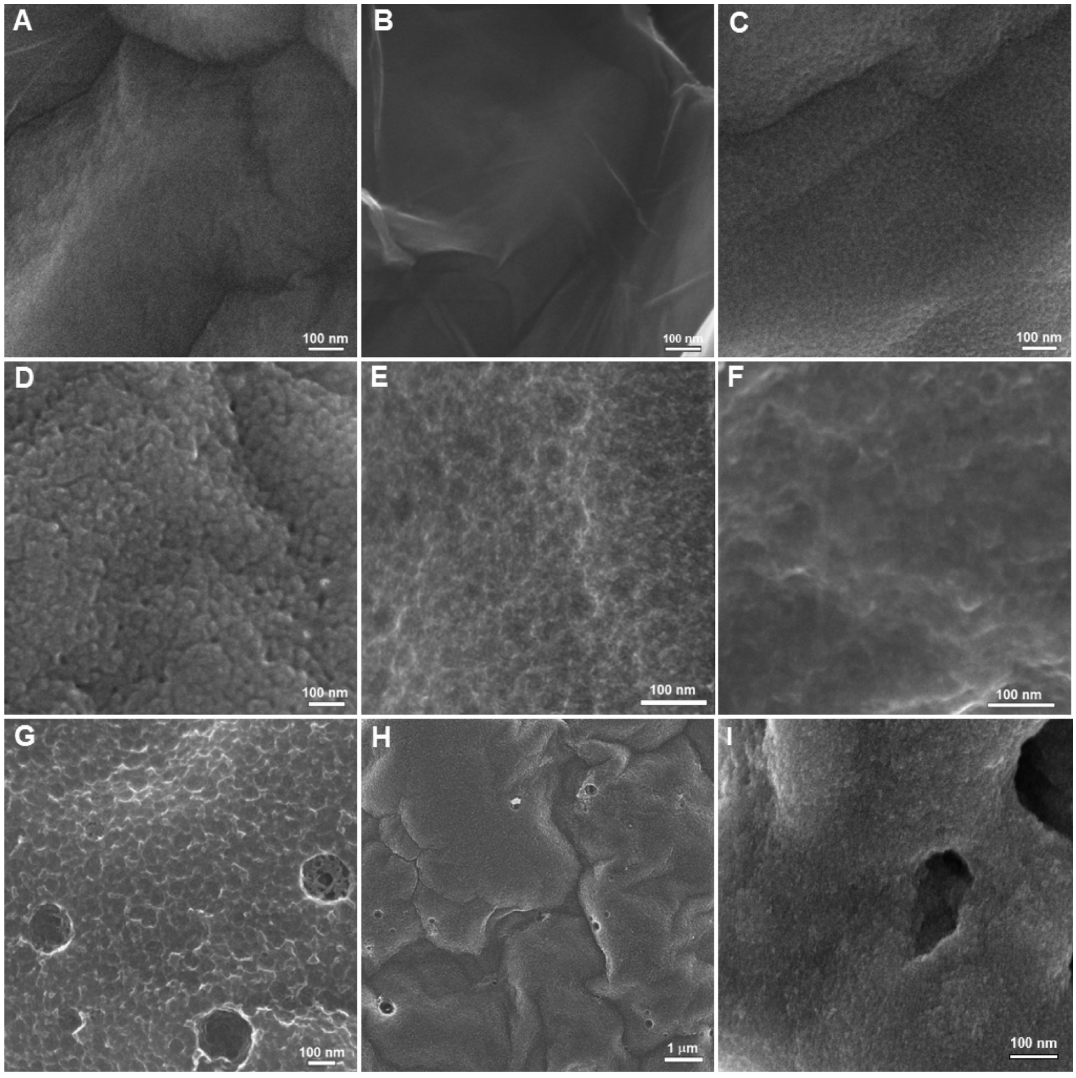

Figure 4. SEM images of the top surface of reduced graphene oxide papers: (A) Ar-rGO, (B) H-rGO, (C) Ar-rHGO-I, (D) Ar-rHGO-II, (E) Ar-rHGO-III, (F) H-rHGO-III, (G) Ar-rHGO-IV, (H) Ar-rHGO-IV at low magnification, (I) H-rHGO-IV.

than the H-rHGO papers. HRTEM of a crushed rHGO paper showed visible porosity in the thin (few-layer thick) regions close to the edge of a reconstituted stack (Figure 6A).

All rHGO papers displayed a (002) X-ray diffraction peak at ~26° 2θ on top of a broad hump, suggesting the presence of both crystalline graphitic and disordered graphene phases (Figure 6B). The peak was more distinct for the H-rHGO than the Ar-rHGO samples, indicating larger graphitic domains. For Ar-rHGO-IV, there might be a slight shift to a lower angle, corresponding to an expansion of the (002) interlayer spacing from 3.35 to 3.56 Å. This could indicate, on the average, a reduced van der Waals attraction between the highly porous rHGO layers. Importantly, the rHGO papers exhibited insignificant deterioration in electrical conductivity compared to rGO (Table 1).

The surface areas and pore volume of Ar-rHGO-III, the sample that demonstrated the best electrochemical performance (see below), were compared with Ar-rGO. The BET surface areas were 15 and 25 m^2/g for Ar-rHGO-III and Ar-rGO, respectively, and the BJH pore volumes were 0.393 and 0.058 cm^3/g. For both samples, there was substantial pore volume in the 30−50 nm region, although the large majority of the pore volume was due to macropores larger than 50 nm. The much larger pore volume in rHGO is consistent with the notion that the presence of in-plane porous defects facilitates access to the internal volumes of the reduced graphene paper.

The electrochemical performance of rHGO papers with a thickness of ~5 μm was examined using galvanostatic charge/discharge measurements in the voltage range of 0.02−1.5 V at various current densities from 50 mA/g (C/7.4 based on a theoretical capacity of 372 mAh/g) to 2000 mA/g (5.4C) (Figure 7 and Table 2). None of the rHGO papers or rGO displayed distinct voltage plateaus, indicating hard carbon with electronically and geometrically nonequivalent sites,[45] and the rHGO papers exhibited less polarization (Figure 7A and B).

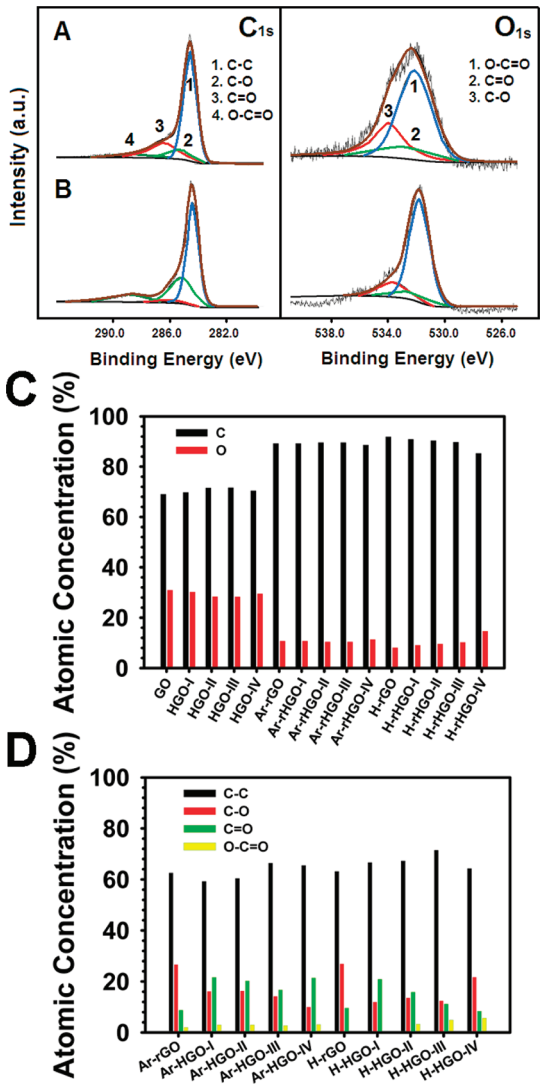

Figure 5. Deconvoluted C1s and O1s XPS spectra of (A) Ar-rHGO-IV and (B) H-rHGO-IV papers. The oxygen content was ~13 and 15 wt % for Ar- and H_2-reduced HGO-IV, respectively. (C) Atomic concentrations of C and O obtained by calculating the ratio of the total area of C1s and O1s XPS components. The oxygen content was ~12 wt % for Ar-rGO to Ar-rHGO-III and 8−10 wt % for H-rGO to H-rHGO-III. (D) Atomic concentrations of various forms of C in various GO, HGO, rGO, and rHGO papers, obtained by integrating the C1s XPS peak areas corresponding to the sp^2 carbon, C−O, C═O, and O−C═O bonded carbon.

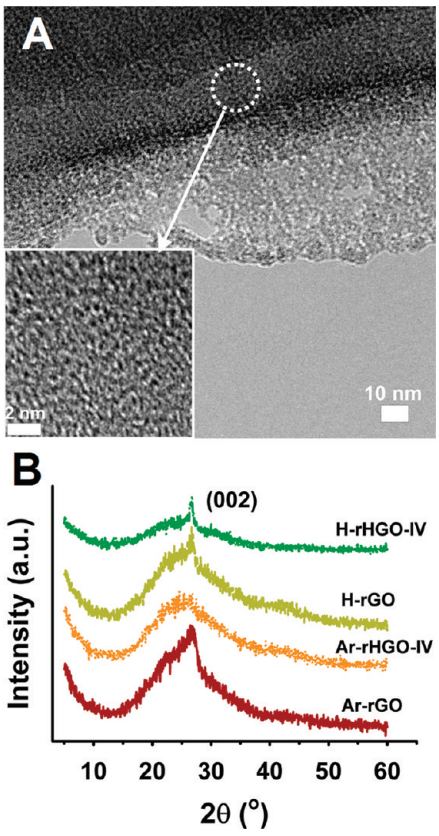

Figure 6. (A) HRTEM image of crushed Ar-rHGO-III showing the porous structure on the thin (few-layer thick) region near the edges of the sheet. Inset shows the basal planes of the graphitic domain at a higher magnification. (B) X-ray diffraction patterns of rGO and rHGO-IV papers.

The Ar-rHGO and H-rHGO papers displayed a ~60% and 30% increase in the irreversible capacity in the first cycle compared with Ar-rGO and H-rGO, respectively. This can be ascribed to two factors. First, the larger densities of residual surface functional groups in rHGO led to more extensive side reactions of Li ions with these oxygen- and hydrogen-containing groups.[45−49] Second, the highly active carbon radicals at the defect sites[50] promoted initial electrolyte decomposition at the electrode/electrolyte interface and the formation of solid electrolyte interphase (SEI) film.[51] The more accessible surface of rHGO facilitated by the in-plane pores would lead to a higher irreversible capacity due to more extensive formation of a passivation surface film. The irreversible capacity of Ar-rHGO was slightly higher than that of the H-rHGO counterparts due to its higher oxygen content and larger pores.

Beyond the first cycle, the rHGO papers displayed higher delithiation capacities than rGO in the entire rate test (Table 2). The marked increase in Li storage capacity with increasing severity of acid treatment was evident when the rate was higher than 1C. Beyond the first 20 cycles, the Coulombic efficiencies were 99.8 ± 0.2%. The best capacity retention at high rates was achieved in Ar-rHGO-III among the Ar-reduced samples, with a reversible capacity of 180 mAh/g, two times higher than that of Ar-rGO at 5.4C. On the other hand, H-rHGO-II showed the highest capacity among the H_2-reduced series, with 4 times higher reversible capacity at 5.4C than H-rGO. The capacity of all the electrodes showed little degradation upon prolonged cycling after the first couple of cycles (Figure 7C). For Ar-rHGO-III, tests at 13.3C and 26.6C revealed no capacity loss up to 1000 cycles (Figure 8D). A performance comparison of rGO and rHGO cells with various energy storage techniques[52] is highlighted in the Ragone plot in Figure 8. The specific power of Ar-rHGO-III, calculated by integrating the charge curves, was more than

TABLE 1. Sheet Resistance and Electrical Conductivity of rGO and rHGO Papers

reduction atmosphere	sample	sheet resistance (ohm/square)	resistivity (ohm cm)	conductivity (S/cm)
Ar	rGO	10	5.0×10^{-3}	2.0×10^{2}
	rHGO-I	7.2	3.6×10^{-3}	2.8×10^{2}
	-II	18	9.0×10^{-3}	1.1×10^{2}
	-III	20	9.8×10^{-3}	1.0×10^{2}
	-IV	26	1.3×10^{-2}	7.7×10^{1}
H_2/Ar	rGO	10	5.0×10^{-3}	2.0×10^{2}
	rHGO-I	11	5.6×10^{-3}	1.8×10^{2}
	-II	16	7.8×10^{-3}	1.3×10^{2}
	-III	15	7.4×10^{-3}	1.4×10^{2}
	-IV	16	7.8×10^{-3}	1.3×10^{2}

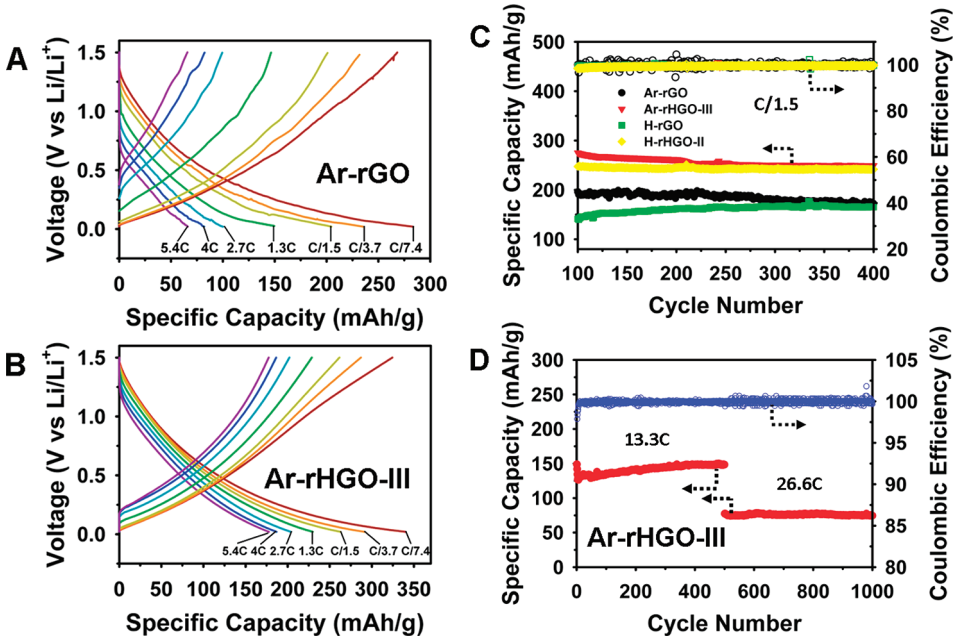

Figure 7. Electrochemical characterization of ~5 μm thick rGO and rHGO paper electrodes: comparison of fifth-cycle charge/discharge curves of (A) Ar-rGO and (B) Ar-rHGO-III between 0.02 and 1.5 V at current densities of 50, 100, 200, 500, 1000, 1500, and 2000 mA/g (C/7.4, C/3.7, C/1.5, 1.3C, 2.7C, 4C, and 5.4C based on a theoretical capacity of 372 mAh/g of graphitic materials); (C) extended cycling tests of rGO, Ar-rHGO-III, and H-rHGO-II at C/1.5 after the tests in Table 2; (D) extended cycling tests of Ar-rHGO-III at 5 A/g (13.3C) and 10 A/g (26.6C).

1 order of magnitude higher than that of Ar-rGO and comparable to that of supercapacitors while having orders of magnitude larger energy density.

From the characterization results, the major difference between rGO and the rHGO samples was the porosity. Therefore, the significantly improved Li-ion storage capacity and rate capability of the latter can be attributed to the introduction of in-plane pores that provided much more accessible interior volumes and enhanced Li-ion diffusion. The Ar-rHGO papers exhibited higher capacity than the H-rHGO counterparts, probably due to their larger pore sizes. They also possessed a larger abundance of oxygen groups, which are likely electrochemically active and could contribute to reversible storage capacity and initial irreversible losses.[49,53] The fact that there was an optimal acid treatment and resulting pore size is interesting. The maximum specific capacity of over 400 mAh/g and capacity retention of >30% at 5.4C were observed in Ar-rHGO-III and H-rHGO-II, which reveal an optimal in-plane pore size of 20−70 nm. Beyond the optimum, further increase of the pore size lowered the storage capacity, especially at high rates. It is likely a consequence of a combination of factors, which include the different nature of SEI layers, in-plane porosity, and interlayer voids for Li-ion diffusion and storage, as well as binding of Li at defect and edge sites. More studies are now underway to fully understand this phenomenon.

Electrochemical impedance spectroscopy (EIS) confirmed a remarkably improved charge-transfer and Li-ion diffusion kinetics in the rHGO than the rGO papers. Nyquist plots of all the rHGO papers showed a broad depressed semicircle at frequencies above 10 Hz for

TABLE 2. Delithiation Capacity of rGO and rHGO Paper Electrodes: Irreversible Capacity of the First Cycle, C_{Irr}, at C/7.4 and Reversible Capacity of the Second Cycle, C_{Re}, at Various Current Densities[a]

			rate						
		C_{Irr} (mAh/g)	C_{Re} (mAh/g)						
reduction atmosphere	sample	C/7.4	C/7.4	C/3.7	C/1.5	1.3C	2.7C	4C	5.4C
Ar	rGO	504	336	232	201	147	100	82	66
	rHGO-I	891	459	280	238	193	147	136	111
	-II	743	400	272	241	206	169	148	135
	-III	819	403	287	261	230	203	187	178
	-IV	908	408	258	230	197	158	130	112
H_2/Ar	rGO	535	313	221	186	136	76	32	26
	rHGO-I	562	399	283	242	185	128	95	77
	-II	684	437	286	248	210	165	138	123
	-III	681	454	301	257	198	141	116	97
	-IV	569	429	297	242	174	115	84	66

[a] Data collected starting with C/7.4, then increasing C rate stepwise, collecting data for 10 cycles at each rate. Except for the first 20 cycles at C/7.4 and C/3.7, the capacity was constant and the Coulombic efficiency was 99.8 ± 0.2%. After 5.4C, the rate was reduced to C/1.5, and the capacity was identical to the earlier value within ±5%. Data extracted from ref 40.

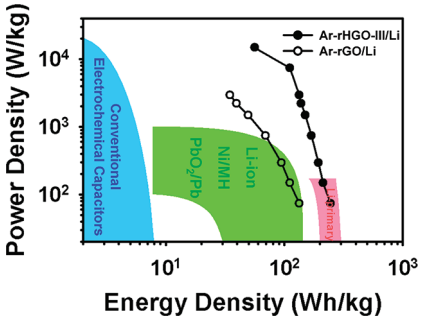

Figure 8. Ragone plot of power density *versus* energy density for Ar-rGO and Ar-rHGO-III electrodes *versus* Li metal foil, together with other energy storage technologies, replotted from ref 52. The specific power and energy density were calculated by integrating the charge curves in parts A and B of Figure 7, based on the masses of rGO and rHGO electrodes.

the charge-transfer kinetic-controlled region and a straight line at frequencies below 10 Hz for the mass-transfer-controlled Warburg region (Figure 9).[54] The semicircles at high frequency before and after cycling shrunk gradually from rGO to rHGO-IV, indicating a substantial decrease of charge-transfer resistance with increasing pore size and/or density. The phase angle of the Warburg region showed no obvious trend before cycling, possibility due to different degrees of wetting (Figure 9A). After cycling, rHGOs displayed larger phase angles, suggesting lower ion diffusion resistance compared with rGO (Figure 9B). These data were quantified by fitting to a typical equivalent circuit for battery

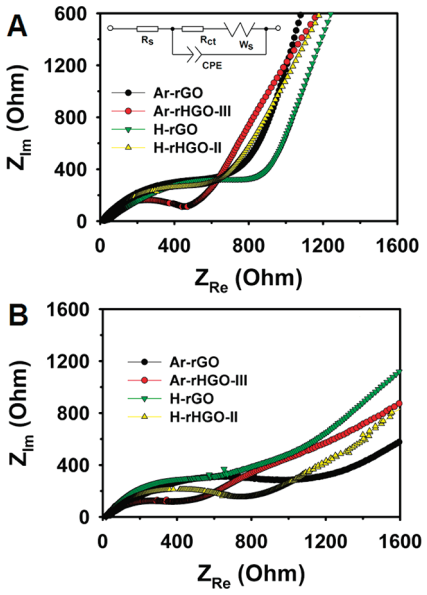

Figure 9. Nyquist plots of rGO and optimal rHGO paper electrodes (A) before and (B) after 10 cycles at 1000 mA/g. Inset in (A) shows the equivalent circuit for the electrodes. R_s is equivalent circuit resistance, R_{ct} is charge-transfer resistance, CPE is constant phase element referring to an electric double-layer capacitance of nonhomogeneous systems, and W_s is the Warburg element, referring to a one-dimensional diffusion resistance.

electrodes (inset in Figure 9A), and the resulting charge-transfer resistance, constant phase element, and Warburg coefficient are shown in Table 3.

The low-rate reversible capacities of our rHGO papers were slightly higher than that of the natural graphite[55] and approximately that of the recently reported thermally/chemically reduced GO[7,26,27,56,57] and GO nanoribbons,[58] while larger reversible capacities of 600−1200 mAh/g have been reported in curled and disordered graphene.[59,60] At least 100 mAh/g, and likely more, of the difference could be attributed to the narrower voltage range used in our testing, 0.02−1.5 V, *versus* 0.005−0.010 to 3.0−3.5 V used in the literature. It is also known that the electrochemical performance of graphene is strongly dependent on the processing procedure, which affects the specific surface area, interlayer spacing, layer stacking, distribution, *etc.*, of graphene.[26,28,60,61] Thus the relatively low content of surface groups and/or low degree of stacking fault could be responsible for the lower capacities in our case. Nevertheless, the ability of our holey graphene paper electrodes to retain the storage capacity at high rates should be noted. Over one-third of the storage capacity was retained for a 10-fold increase in rate, outperforming many other carbon-based flexible electrodes.[5,27,62,63] Furthermore, the protocol we developed here could be readily applied to other forms of highly capacitive graphene, and a more pronounced improvement of reversible capacity could be expected by further maximizing the availability of graphene edges and incorporating other high-capacity active species into the graphene matrix.

TABLE 3. Calculated Charge-Transfer Resistance, Constant Phase Element, and Warburg Coefficient (at $f = 0.16$ Hz) of rGO and rHGO Paper Electrodes

		before cycling			after cycling		
reduction atmosphere	sample	charge-transfer resistance (ohm)	constant phase element (farad)	Warburg coeff (ohm $s^{-1/2}$)	charge-transfer resistance (ohm)	constant phase element (farad)	Warburg coeff (ohm $s^{-1/2}$)
Ar	rGO	551	8.6×10^{-5}	9.1×10^{3}	693	3.1×10^{-5}	2.5×10^{3}
	rHGO-I	540	1.7×10^{-5}	3.1×10^{3}	649	3.1×10^{-5}	2.2×10^{3}
	-II	535	1.1×10^{-5}	2.5×10^{3}	524	1.6×10^{-5}	1.3×10^{3}
	-III	516	2.5×10^{-5}	4.2×10^{3}	500	1.8×10^{-5}	1.1×10^{3}
	-IV	460	4.1×10^{-5}	8.1×10^{2}	436	3.1×10^{-5}	7.3×10^{2}
H_2/Ar	rGO	770	5.3×10^{-5}	6.1×10^{3}	689	1.7×10^{-5}	2.2×10^{3}
	rHGO-I	582	1.9×10^{-5}	5.2×10^{3}	550	9.9×10^{-6}	2.5×10^{3}
	-II	548	1.1×10^{-5}	8.3×10^{3}	656	5.5×10^{-6}	1.9×10^{3}
	-III	430	1.5×10^{-5}	6.2×10^{3}	642	3.7×10^{-6}	2.1×10^{3}
	-IV	430	2.1×10^{-5}	7.6×10^{2}	372	3.1×10^{-6}	8.9×10^{2}

CONCLUSIONS

A wet chemistry approach has been applied to generate porosity on the basal planes of graphene in a controlled manner. Highly conducting, self-supporting paper electrodes, composed of a 3-D continuous graphene phase and graphitic domains reconstituted from these holey graphene sheets, exhibit much enhanced Li-ion storage capacity and transport properties than without the holey defects, while not adversely affecting the electrical conductivity or ductility. The microscopic engineering we have devised on graphene presents an attractive and facile improvement for graphitic electrodes, achieving an ultrahigh rate capability that is comparable to those of supercapacitors. In addition, the protocol used can be readily extended to rational designs of graphene-based composite materials, and the free-standing graphene sheets with tunable porosity may find other applications such as curvilinear electronics, transfer membranes, and supporting scaffolds.

EXPERIMENTAL SECTION

Synthesis of Graphene Oxide (GO). GO was synthesized from flake graphite (Asbury Carbons, 230U grade, high-carbon natural graphite 99^{+}) by a modified Hummers method.[36] The graphite powder (2.0 g) was preoxidized by stirring it into a concentrated H_2SO_4 (20 mL) solution in which $K_2S_2O_8$ (1.0 g) and P_2O_5 (1.0 g) were completely dissolved at 80 °C. The mixture, in a beaker, was kept at 80 °C for 4.5 h using an oil bath. After the mixture was cooled and diluted with 1 L of DDI (distilled deionized) water, the pretreated product was filtered with a Nylon membrane filter (47 mm diameter, 0.2 μm pore size, Millipore) and washed on the filter until the pH of filtrate water became neutral. The shiny, dark gray, preoxidized graphite was dried in air overnight. Then it was dispersed by stirring into chilled H_2SO_4 (75 mL) in an Erlenmeyer flask in an ice bath. $KMnO_4$ (10 g) was added slowly with stirring to keep the temperature of reaction mixture below 20 °C. The resulting thick, dark green paste was allowed to react at 35 °C for 2 h followed by addition of DDI water (160 mL) to form a dark brown solution. To avoid overflow of the mixture due to rapid temperature rise with foaming by water addition, the flask was chilled in an ice bath and water was added in ~5 mL aliquots with close monitoring of the temperature (kept below 50 °C). After additional stirring for 2 h, the dark brownish solution was further diluted with distilled water (500 mL), and H_2O_2 (30%, 8.3 mL) was added slowly. The color of the mixture turned bright yellow. The mixture was allowed to settle overnight. The supernatant was decanted, and the remaining product was repeatedly centrifuged and washed with DDI water until the pH of the solution became neutral. (At this stage, the Mn concentration in the supernatant was below 0.1 ppm by AAS.) Then, the obtained product was diluted to make a ~0.5% w/w aqueous dispersion for storage.

Synthesis of Holey GO (HGO). Two milliliters of the above aqueous GO suspension was diluted to ~0.1% w/w by DDI water and mixed with the desired amount of 70% concentrated HNO_3 in a sealed 20 mL glass vial under stirring. The mixture was sonicated in a bath sonicator (100 W, 50/60 Hz) at room temperature for 1 h. Four different concentrations of HNO_3 were tested, corresponding to a GO suspension/70% HNO_3 volume ratio of 1:5 (I), 1:7.5 (II), 1:10 (III), and 1:12.5 (IV). After sonication, the mixture was settled at room temperature for an hour and then poured into 100 mL of water, centrifuged at 20 000 rpm, and washed with water to remove the acid. The resulting holey GO paper containing in-plane carbon vacancies are labeled HGO and were obtained by filtering the resulting purified aqueous suspension through an Anodisc membrane filter (47 mm diameter, 0.2 μm pore size, Whatman), followed by air drying and peeling from the filter.

Reduction of GO and HGO Papers. GO or HGO papers were cut by a razor blade into smaller ribbons so as to fit into a quartz tube for thermal reduction. The GO or HGO papers were reduced with either a flow of Ar (~90 mL min^{-1}) or 10% hydrogen in argon (~100 mL min^{-1} total flow) at 700 °C for 1 h. The reduced samples are labeled rGO or rHGO.

Structural Characterization. The morphology and thickness of as-prepared HGO and rHGO samples were investigated using Hitachi S-4800-II field emission scanning electron microscopy (FE-SEM) and JEOL 2100F field emission transmission electron microscopy (FE-TEM). To perform ion-exchange of HGO with Pd^{2+}, an appropriate amount of $Pd(OAc)_2$ was dissolved in DDI water and allowed to settle for hours. After removing the insoluble matter, the supernatant or further diluted supernatant of $Pd(OAc)_2$ was stirred with an aqueous (de)GO dispersion overnight. The ion-exchanged HGO was loaded onto a sample holder for the Hitachi HD-2300A FE-STEM operated at 200 kV with energy dispersive spectroscopy (EDS) detectors. X-ray

diffraction (XRD) patterns of rHGO papers were collected by a Scintag XDS2000 diffractometer with Cu Kα radiation (λ = 1.5418 Å) at 40 kV, a step size of 0.01°, and a step time of 0.5 s. X-ray photoelectron spectroscopy (XPS) of rHGO papers was performed using an Omicron ESCA probe equipped with an electron flood gun. The Al Kα radiation (1486.6 eV) was used as an excitation source, and the binding energy scale was calibrated with respect to adventitious carbon (C1s). Sheet resistance measurements were made on ~5 μm thick, coin cell-size circular rHGO papers with a four-point probe technique and an electrode separation of 1 mm using a Keithley 2400 sourcemeter at room temperature. The sheet resistance was calculated using the formula $R_s = Ka(s/t)(V/I)2\pi$, where s is the electrode spacing, t is the sample thickness. $K = 0.9628$ and $a = 0.721(t/s)$ are geometric correction factors. Resistivity and conductivity were calculated as $\rho = R_s t$ and $\sigma = 1/\rho$. N_2 adsorption and desorption isotherms at 77 K were collected using Micromeritics ASAP 2000, after degassing the samples at 350 °C for 2 h. Surface area and pore volumes were determined using the BET and BJH methods, respectively.

Electrochemical Test. Electrochemical measurements were carried out on rHGO papers using two-electrode coin cells with Li metal as the counter electrode. The rHGO working electrodes were typically 0.2−0.3 mg cm^{-2} and ~5 μm thick. A microporous glass-fiber membrane (Whatman) was used as separator, and a Cu foil (99.999%, 0.025 mm thick, Alfa-Aesar) was employed to connect the rHGO papers to external leads. The electrolyte consisted of 1 M $LiPF_6$ in ethylene carbonate (EC)/dimethyl carbonate (DMC) (1:1, v/v). The cells were assembled in an argon-filled glovebox, and galvanostatic measurements were conducted with a BT2000 potentiostat/galvanostat system (Arbin Instruments) at various current densities, typically in the voltage range 0.02−1.5 V *vs* Li/Li$^+$. Electrochemical impedance spectroscopy measurements were conducted on two-electrode Swagelok-type cells with a Li metal counter electrode and 120 μL of the above electrolyte. Data were collected using a Solartron 1260 impedance analyzer coupled with a Solartron 1286 electrochemical interface by applying an ac voltage of 10 mV amplitude and dc open circuit voltage in the frequency range 1 MHz to 0.01 Hz at room temperature.

Acknowledgment. This research was supported by the Center for Electrical Energy Storage, an Energy Frontier Research Center funded by the U.S. Department of Energy, Office of Science and Office of Basic Energy Sciences, grant no. DE-AC02-06CH11357.

REFERENCES AND NOTES

1. Liang, M.; Zhi, L. Graphene-Based Electrode Materials for Rechargeable Lithium Batteries. *J. Mater. Chem.* **2009**, *19*, 5871–5875.
2. Zhu, Y.; Murali, S.; Cai, W.; Li, X.; Suk, J. W.; Potts, J. R.; Ruoff, R. S. Graphene and Graphene Oxide: Synthesis, Properties, and Applications. *Adv. Mater.* **2010**, *22*, 3906–3924.
3. Chen, D.; Tang, L.; Li, J. Graphene-Based Materials in Electrochemistry. *Chem. Soc. Rev.* **2010**, *39*, 3157–3180.
4. YuanC. Z.; Gao, B.; Shen, L. F.; Yang, S. D.; Hao, L.; Lu, X. J.; Zhang, L. J.; Zhang, X. G. Hierarchically Structured Carbon-Based Composites: Design, Synthesis and Their Application in Electrochemical Capacitors. *Nanoscale* **2010**, *3*, 529–545.
5. Brownson, D. A. C.; Kampouris, D. K.; Banks, C. E. An Overview of Graphene in Energy Production and Storage Applications. *J. Power Sources* **2011**, *196*, 4873–4885.
6. Yin, S.; Zhang, Y.; Kong, J.; Zou, C.; Li, C. M.; Lu, X.; Ma, J.; Boey, F. Y. C.; Chen, X. Assembly of Graphene Sheets into Hierarchical Structures for High-Performance Energy Storage. *ACS Nano* **2011**, *5*, 3831–3838.
7. Fan, Z.-J.; Yan, J.; Wei, T.; Ning, G.-Q.; Zhi, L.-J.; Liu, J.-C.; Cao, D.-X.; Wang, G.-L.; Wei, F. Nanographene-Constructed Carbon Nanofibers Grown on Graphene Sheets by Chemical Vapor Deposition: High-Performance Anode Materials for Lithium Ion Batteries. *ACS Nano* **2011**, *5*, 2787–2794.
8. Zhao, X.; Mendoza Sanchez, B.; Dobson, P. J.; Grant, P. S. The Role of Nanomaterials in Redox-Based Supercapacitors for Next Generation Energy Storage Devices. *Nanoscale* **2011**, *3*, 839–855.
9. Wang, D.-W.; Li, F.; Zhao, J.; Ren, W.; Chen, Z.-G.; Tan, J.; Wu, Z.-S.; Gentle, I.; Lu, G. Q.; Cheng, H.-M. Fabrication of Graphene/Polyaniline Composite Paper *via In Situ* Anodic Electropolymerization for High-Performance Flexible Electrode. *ACS Nano* **2009**, *3*, 1745–1752.
10. Wu, Z.-S.; Ren, W.; Wang, D.-W.; Li, F.; Liu, B.; Cheng, H.-M. High-Energy MnO_2 Nanowire/Graphene and Graphene Asymmetric Electrochemical Capacitors. *ACS Nano* **2010**, *4*, 5835–5842.
11. Kuilla, T.; Bhadra, S.; Yao, D.; Kim, N. H.; Bose, S.; Lee, J. H. Recent Advances in Graphene Based Polymer Composites. *Prog. Polym. Sci.* **2010**, *35*, 1350–1375.
12. Reddy, A. L. M.; Srivastava, A.; Gowda, S. R.; Gullapalli, H.; Dubey, M.; Ajayan, P. M. Synthesis of Nitrogen-Doped Graphene Films for Lithium Battery Application. *ACS Nano* **2011**, *4*, 6337–6342.
13. Wu, Z.-S.; Ren, W.; Xu, L.; Li, F.; Cheng, H.-M. Doped Graphene Sheets as Anode Materials with Superhigh Rate and Large Capacity for Lithium Ion Batteries. *ACS Nano* **2011**, *5*, 5463–5471.
14. Guo, Y.; Guo, S.; Ren, J.; Zhai, Y.; Dong, S.; Wang, E. Cyclodextrin Functionalized Graphene Nanosheets with High Supramolecular Recognition Capability: Synthesis and Host-Guest Inclusion for Enhanced Electrochemical Performance. *ACS Nano* **2011**, *4*, 4001–4010.
15. Geim, A. K.; Novoselov, K. S. The Rise of Graphene. *Nat. Mater.* **2007**, *6*, 183–191.
16. Kumar, A.; Zhou, C. The Race to Replace Tin-Doped Indium Oxide: Which Material Will Win? *ACS Nano* **2010**, *4*, 11–14
17. Lee, C.; Wei, W.; Kysar, J. W.; Hone, J. Measurement of the Elastic Properties and Intrinsic Strength of Monolayer Graphene. *Science* **2008**, *321*, 385–388.
18. Hecht, D. S.; Hu, L.; Irvin, G. Emerging Transparent Electrodes Based on Thin Films of Carbon Nanotubes, Graphene, and Metallic Nanostructures. *Adv. Mater.* **2011**, *23*, 1482–1513.
19. Paek, S.-M.; Yoo, E.; Honma, I. Enhanced Cyclic Performance and Lithium Storage Capacity of SnO_2/Graphene Nanoporous Electrodes with Three-Dimensional Delaminated Flexible Structure. *Nano Lett.* **2009**, *9*, 72–75.
20. Yang, S.; Feng, X.; Ivanovici, S.; Muellen, K. Fabrication of Graphene-Encapsulated Oxide Nanoparticles: Towards High-Performance Anode Materials for Lithium Storage. *Angew. Chem., Int. Ed.* **2010**, *49*, 8408–8412.
21. Wu, Z.-S.; Ren, W.; Wen, L.; Gao, L.; Zhao, J.; Chen, Z.; Zhou, G.; Li, F.; Cheng, H.-M. Graphene Anchored with Co_3O_4 Nanoparticles as Anode for Lithium Ion Batteries with Enhanced Reversible Capacities and Cycling Performance. *ACS Nano* **2010**, *4*, 3187–3194.
22. Lee, J. K.; Smith, K. B.; Hayner, C. M.; Kung, H. H. Silicon Nanoparticles-Graphene Paper Composites for Li Ion Battery Anodes. *Chem. Commun.* **2010**, *46*, 2025–2027.
23. Li, D.; Kaner, R. B. Graphene-Based Materials. *Science* **2008**, *320*, 1170–1171.
24. Yoo, E.; Kim, L.; Hosono, E.; Zhou, H.-S.; Kudo, T.; Honma, I. Large Reversible Li Storage of Graphene Nanosheet Families for Use in Rechargeable Lithium Ion Batteries. *Nano Lett.* **2008**, *8*, 2277–2282.
25. Uthaisar, C.; Barone, V. Edge Effects on the Characteristics of Li Diffusion in Graphene. *Nano Lett.* **2010**, *10*, 2838–2842.
26. Pan, D.; Wang, S.; Zhao, B.; Wu, M.; Zhang, H.; Wang, Y.; Jiao, Z. Li Storage Properties of Disordered Grapehen Nanosheets. *Chem. Mater.* **2009**, *21*, 3136–3142.
27. Abouimrane, A.; Compton, O. C.; Amine, K.; Nguyen, S. T. Non-Annealed Graphene Paper as a Binder-Free Anode for Lithium-Ion Batteries. *J. Phys. Chem. C* **2010**, *114*, 12800–12804.
28. Stoller, M. D.; Park, S.; Zhu, Y.; An, J.; Ruoff, R. S. Graphene-Based Ultracapacitors. *Nano Lett.* **2008**, *8*, 3498–3502.
29. Miller, J. R.; Outlaw, R. A.; Holloway, B. C. Graphene Double-Layer Capacitor with ac Line-Filtering Performance. *Science* **2010**, *329*, 1637–1639.

30. Yoo, J. J.; Balakrishnan, K.; Huang, J.; Meunier, V.; Sumpter, B. G.; Srivastava, A.; Conway, M.; Reddy, A. L. M.; Yu, J.; Vajtai, R.; *et al*. Ultrathin Planar Graphene Supercapacitors. *Nano Lett.* **2011**, *11*, 1423–1427.
31. Liu, C.; Yu, Z.; Neff, D.; Zhamu, A.; Jang, B. Z. Graphene-Based Supercapacitor with an Ultrahigh Energy Density. *Nano Lett.* **2010**, *10*, 4863–4868.
32. Harris, P. J. F.; Green, M. L. H.; Tsang, S. C. High-Resolution Electron Microscopy of Tubule-Containing Graphitic Carbon. *J. Chem. Soc., Faraday Trans.* **1993**, *89*, 1189–1192.
33. Liu, J.; Rinzler, A. G.; Dai, H.; Hafner, J. H.; Bradley, R. K.; Boul, P. J.; Lu, A.; Iverson, T.; Shelimov, K.; Huffman, C. B.; *et al*. Fullerene Pipes. *Science* **1998**, *280*, 1253–1256.
34. Farkas, E.; Anderson, M. E.; Chen, Z.; Rinzler, A. G. Length Sorting Cut Single Wall Carbon Nanotubes by High Performance Liquid Chromatography. *Chem. Phys. Lett.* **2002**, *363*, 111–116.
35. Wang, S.; Tang, L. A. L.; Bao, Q.; Lin, M.; Deng, S.; Goh, B. M.; Loh, K. P. Room-Temperature Synthesis of Soluble Carbon Nanotubes by the Sonication of Graphene Oxide Nanosheets. *J. Am. Chem. Soc.* **2009**, *131*, 16832–16837.
36. Kovtyukhova, N. I.; Ollivier, P. J.; Martin, B. R.; Mallouk, T. E.; Chizhik, S. A.; Buzaneva, E. V.; Gorchinskiy, A. D. Layer-by-Layer Assembly of Ultrathin Composite Films from Micron-Sized Graphite Oxide Sheets and Polycations. *Chem. Mater.* **1999**, *11*, 771–778.
37. Mason, T. J.; Lorimer, J. P. *Sonochemistry: Theory, Applications and Uses of Ultrasound in Chemistry*; Halsted: New York, 1988.
38. Hennrich, F.; Krupke, R.; Arnold, K.; Stütz, J. A. R.; Lebedkin, S.; Koch, T.; Schimmel, T.; Kappes, M. M. The Mechanism of Cavitation-Induced Scission of Single-Walled Carbon Nanotubes. *J. Phys. Chem. B* **2007**, *111*, 1932–1937.
39. Forrest, G. A.; Alexander, A. J. A Model for the Dependence of Carbon Nanotube Length on Acid Oxidation Time. *J. Phys. Chem. C* **2007**, *111*, 10792–10798.
40. Zhao, X.; Hayner, C. M.; Kung, M. C.; Kung, H. H. In-Plane Vacancy-Enabled High-Power Si-Graphene Composite Electrode for Lithium-Ion Batteries. *Adv. Energy Mater.* **2011**, DOI: 10.1002/aenm.201100426.
41. Gao, W.; Alemany, L. B.; Ci, L.; Ajayan, P. M. New Insights into the Structure and Reduction of Graphite Oxide. *Nat. Chem.* **2009**, *1*, 403–408.
42. Yang, D.; Velamakanni, A.; Bozoklu, G.; Park, S.; Stoller, M.; Piner, R. D.; Stankovich, S.; Jung, I.; Field, D. A.; Ventrice, C. A., Jr.; *et al*. Chemical Analysis of Graphene Oxide Films after Heat and Chemical Treatments by X-Ray Photoelectron and Micro-Raman Spectroscopy. *Carbon* **2009**, *47*, 145–152.
43. Bagri, A.; Mattevi, C.; Acik, M.; Chabal, Y. J.; Chhowalla, M.; Shenoy, V. B. Structural Evolution During the Reduction of Chemically Derived Graphene Oixde. *Nat. Chem.* **2010**, *2*, 581–587.
44. Banhart, F.; Kotakoski, J.; Krasheninnikov, A. V. Structural Defects in Graphene. *ACS Nano* **2011**, *5*, 26–41.
45. Pistoia, G. *Lithium Batteries: New Materials, Developments and Perspectives*; Elsevier, Amsterdam, 1994.
46. Zheng, T.; Liu, Y.; Fuller, E. W.; Tseng, S.; Sacken, U. V.; Dahn, J. R. Lithium Insertion in High Capacity Carbonaceous Materials. *J. Electrochem. Soc.* **1995**, *142*, 2581–2590.
47. Papanek, P.; Radosavljević, M.; Fischer, J. E. Lithium Insertion in Disordered Carbon-Hydrogen Alloys: Intercalation *vs* Covalent Binding. *Chem. Mater.* **1996**, *8*, 1519–1526.
48. Zheng, T.; Xue, J. S.; Dahn, J. R. Lithium Insertion in Hydrogen-Containing Carbonaceous Materials. *Chem. Mater.* **1996**, *8*, 389–393.
49. Zhou, H.; Zhu, S.; Hibino, M.; Honma, I.; Ichihara, M. Lithium Storage in Ordered Mesoporous Carbon (CMK-3) with High Reversible Specific Energy Capacity and Good Cycling Performance. *Adv. Mater.* **2003**, *15*, 2107–2111.
50. Walker Jr., P. L. *Chemistry and Physics of Carbon*; Dekker: New York, 1966; p 251.
51. Balbuena, P. B.; Wang, Y. *Lithium Ion Batteries — Solid Electrolyte Interphase*; Imperial College Press: London, 2004; pp 1—69.
52. Simon, P.; Gogotsi, Y. Materials for Electrochemical Capacitors. *Nat. Mater.* **2008**, *7*, 845–854.
53. Frackowiak, E.; Béguin, F. Carbon Materials for the Electrochemical Storage of Energy in Capacitors. *Carbon* **2001**, *39*, 937–950.
54. Barsoukov, E.; MacDonald, R. *Impedance Spectroscopy: Theory, Experiment, and Applications*, 2nd ed.; John Wiley & Sons: Chichester, UK, 2005; p 84.
55. Yoshio, M.; Brodd, R. J.; Kozawa, A. *Lithium-Ion Batteries: Science and Technologies*; Springer: New York, 2009; pp 63—68.
56. Kim, H.; Kim, S.-W.; Park, Y.-U.; Gwon, H.; Seo, D.-H.; Kim, Y.; Kang, K. SnO_2/Graphene Composite with High Lithium Storage Capability for Lithium Rechargeable Batteries. *Nano Res.* **2010**, *3*, 813–821.
57. Kim, H.; Seo, D.-H.; Kim, S.-W.; Kim, J.; Kang, K. Highly Reversible Co_3O_4/Graphene Hybrid Anode for Lithium Rechargeable Batteries. *Carbon* **2011**, *49*, 326–332.
58. Bhardwaj, T.; Antic, A.; Pavan, B.; Barone, V.; Fahlman, B. D. Enhanced Electrochemical Lithium Storage by Graphene Nanoribbons. *J. Am. Chem. Soc.* **2010**, *132*, 12556–12558.
59. Guo, P.; Song, H.; Chen, X. Electrochemical Performance of Graphene Nanosheets as Anode Material for Lithium-Ion Batteries. *Electrochem. Commun.* **2009**, *11*, 1320–1324.
60. Lian, P.; Zhu, X.; Liang, S.; Li, Z.; Yang, W.; Wang, H. Large Reversible Capacity of High Quality Graphene Sheets as an Anode Material for Lithium-Ion Batteries. *Electrochim. Acta* **2010**, *55*, 3909–3914.
61. Goh, M. S.; Pumera, M. Multilayer Graphene Nanoribbons Exhibit Larger Capacitance than Their Few-Layer and Single-Layer Graphene Counterparts. *Electrochem. Commun.* **2010**, *12*, 1375–1377.
62. Pushparaj, V. L.; Shaijumon, M. M.; Kumar, A.; Murugesan, S.; Ci, L.; Vajtai, R.; Linhardt, R. J.; Nalamasu, O.; Ajayan, P. M. Flexible Energy Storage Devices Based on Nanocomposite Paper. *Proc. Natl. Acad. Sci. U. S. A.* **2007**, *104*, 13574–13577.
63. Hu, L.; Choi, J. W.; Yang, Y.; Jeong, S.; Mantia, F. L.; Cui, L.-F.; Cui, Y. Highly Conductive Paper for Energy Storage Devices. *Proc. Natl. Acad. Sci. U. S. A.* **2009**, *106*, 21490–21494.